Supporting Information for "Large-scale Interseismic Strain Mapping of the NE Tibetan Plateau from Sentinel-1 Interferometry"

Q. Ou[1], S. Daout[1] *, J.R. Weiss[2,3,] †, L. Shen[2], M. Lazecký[2], T.J. Wright[2],

B.E. Parsons[1]

[1]COMET, Department of Earth Sciences, University of Oxford, South Parks Road, Oxford, United Kingdom

[2]COMET, School of Earth and Environment, University of Leeds, Leeds, , United Kingdom

[3]Institute of Geosciences, University of Potsdam, Karl-Liebknecht-Strasse 24, Potsdam, Germany

Contents of this file

1. Text S1 to S6

2. Figures S1 to S20

Corresponding author: Q. Ou, COMET, Department of Earth Sciences, University of Oxford, South Parks Road, Oxford, United Kingdom. (qi.ou@earth.ox.ac.uk)

*Current address, Université de Lorraine - CNRS, UMR 7358, rue N. D. des Pauvres, 54501 Vandœuvre les Nancy, France

†Current address, NOAA/NWS Pacific Tsunami Warning Center, 1845 Wasp Boulevard, Honolulu, Hawaii, USA

Introduction

Texts S1-S3 describe detailed methods for InSAR time series analysis. Fig S1-S2 show the interferogram networks. Figs S3-S4 show quality analysis of atmospheric correction using the GACOS model. Text S4 describe GNSS data available in the study area. Figs S5 shows LOS velocities before they are placed in the GNSS reference frame and the distribution of 2D and 3D GNSS stations in the area. Figs S6-S9 illustrate the method used to stitch InSAR LOS along track and assess the effectiveness of the method. Figs S7, S10 and S13 illustrate the detailed steps in decomposing LOS into Cartesian velocities. Text S5 and Fig S11 describe a method to scale InSAR LOS uncertainty maps to remove the local reference effect. Text S6 and S12 compare an alternative velocity decomposition method with the $V_E - V_{UN}$ decomposition described in the main text. Figs S14 and S16 show synthetic tests that inform the filtering of InSAR V_E for strain rate calculations. Fig S17 compares InSAR V_E before and after filtering. Figs S18 and S19 illustrate estimated uncertainties of the V_E and V_N gradients. Fig S20 shows the correlation between ESRI's land cover classification (Karra et al., 2021) and the InSAR V_U map.

Text S1. Ramp removal

Inverting for a network of ramp parameters directly from the network of interferograms is computational expensive. Therefore, we first invert for the best-fit ramp parameters for each interferogram and, from these ramp parameters, invert for networks of ramp parameters per epoch separately to ensure network closure. The ramp removal takes place in four steps: (1) Mask each interferogram with the filtered coherence file from the LiCSAR outputs to only include pixels with coherence higher than 0.5; (2) Estimate the best-fitting linear ramp parameters, a_{ij}, b_{ij}, c_{ij}, for each interferogram between epochs i and j with a planar ramp of the form $z_{ij} = a_{ij}x + b_{ij}y + c_{ij}$, where (x, y) are pixel positions in radar coordinates and calculate the pixel residuals; (3) Separately invert for three networks of epoch ramp parameters a_k, b_k, c_k at each epoch k that best fit the interferogram ramp parameters a_{ij}, b_{ij}, c_{ij} while ensuring network closure; (4) Remove the planar ramps, $z'_{ij} = (a_j - a_i)x + (b_j - b_i)y + (c_j - c_i)$, reconstructed using the epoch ramp parameters from each interferogram.

The inversion in step (3) is weighted by both the temporal baseline of the interferogram in decimal years, dt, and the root-mean-square of the pixel residuals from planar ramp fitting in step (2), rms. This gives higher weights to interferograms with shorter temporal baselines and lower rms residuals. The exact formulation is as follows:

$$\begin{bmatrix} \frac{1}{\sigma_{12}}a_{12} \\ \vdots \\ \frac{1}{\sigma_{ij}}a_{ij} \\ \vdots \\ \frac{1}{\sigma_{(k-1)k}}a_{(k-1)k} \end{bmatrix} = \begin{bmatrix} \frac{1}{\sigma_{12}} & (-1 & 1 & 0 & \dots & \dots & 0) \\ \vdots & \vdots & \vdots & \vdots & \vdots & \vdots & \vdots \\ \frac{1}{\sigma_{ij}} & (0 & \dots & -1 & 1 & \dots & 0) \\ \vdots & \vdots & \vdots & \vdots & \vdots & \vdots & \vdots \\ \frac{1}{\sigma_{(k-1)k}} & (0 & \dots & \dots & 0 & -1 & 1) \end{bmatrix} \begin{bmatrix} a_1 \\ a_2 \\ \vdots \\ a_i \\ a_j \\ \vdots \\ a_{k-1} \\ a_k \end{bmatrix} \tag{1}$$

$$\text{where} \quad \sigma_{ij} = \frac{1}{w_1} + \frac{1}{w_2}$$
$$w_1 = exp(\frac{-dt_{ij}}{2})$$
$$w_2 = exp(\frac{-rms_{ij}}{rms_{80}}) + 0.01$$

taking the inversion for parameter a as an example; rms_{80} is a constant equal to the 80 percentile of the rms values of all interferograms, which ensures the partial weights, w_1 and w_2, have similar ranges. The same inversion is performed for ramp parameters b and c separately.

The reconstructed ramps may have slightly different ramp parameters than the best-fitting ramps, but this step is necessary to ensure ramps removed do not introduce artificial phase misclosure in the network. In addition, it also avoids overfitting each interferogram which could be biased by tectonic signals, turbulent tropospheric delays, decorrelation noise and unwrapping mistakes. After ramp removal, the flattened interferograms for all frames have an average pixel root-mean-squared value of 2.16 rad (∼4 cm two-way), which represents the amplitude of spatial variation of the data used in the times series.

Text S2. Time series inversion

Time series analysis was performed using the NSBAS program developed by López-Quiroz, Doin, Tupin, Briole, and Nicolas (2009) and Doin et al. (2015). NSBAS solves for the temporal increments of phase changes, $\delta\phi_n$, per pixel and applies an overall smoothed temporal function defined by ϕ_k^s to regularize the problem in case of gaps in the network

(Doin et al., 2015):

$$\forall q \in [1, M] \quad \sum_{n=i}^{n=j-1} \delta\phi_n = \Phi_q \tag{2}$$

$$-\alpha W_1 \phi_1^s = 0 \tag{3}$$

$$\forall k \in [2, N] \quad \alpha W_k \left(\sum_{n=1}^{n=k-1} \delta\phi_n - \phi_k^s \right) = 0 \tag{4}$$

$$\forall k \in [1, N] \quad \gamma \omega_k \partial^2 \phi_k^s / \partial t^2 = 0 \tag{5}$$

where Φ_q is the phase in qth interferogram between epoch numbers $n = i$ and $n = j$; ϕ_k is the cumulative phase increment from the first epoch $\phi_1 = 0$ to ϕ_{k-1}. N is the total number of epochs; M is the total number of interferograms. γ is the smoothing coefficient; ω_k is the average time interval between the 5 epochs used to calculate the second derivative. α is set small enough to only have an impact when there are missing links in the network. W_k can be changed at each iteration to weight the inversion differently. The method also has an option to downsample the data for faster computation.

The full-resolution inversion is carried out in two iterations. The first iteration is weighted by the planar ramp misfit per interferogram obtained from the previous step such that the spatially noisier pixels are weighted less. The residuals between the input interferograms and reconstructed interferograms from the first iteration are used to weight the second iteration such that interferograms that fit poorly temporally into the network have less effect on the final time series. We then added the incremental phase delays, $\delta\phi_n$, assuming $\phi_1 = 0$, to obtain the time series of total phase delay, ϕ_k, for LOS velocity extraction.

Text S3. LOS Velocity Extraction

We extract a linear velocity, V, from the time series with $\phi_k = Vt_k$ also in two iterations, where t_k is the cumulative time from the first epoch (Daout et al., 2017). The first iteration is weighted by $\phi_{RMS_{epoch}}$ from the time series inversion and the RMS residual to the planar ramp misfit of the cumulative displacement at each epoch. This means dates associated with interferograms that poorly fit the reconstructed interferograms and dates with noiser cumulative displacements have less effect on the linear velocity. Then, the misfit per pixel per epoch from the first iteration is added to the weighting parameter for the second iteration of inversion such that the epochs that deviate more from a linear velocity trend are weighted less.

Text S4. GNSS data on the NE Tibetan Plateau

Thanks to the two-phased installation of the CMONOC GNSS network in 1999 and 2009, the NE Tibetan Plateau is well covered by GNSS stations in terms of spatial density and distribution (Gan et al., 2007; Liang et al., 2013; Wang & Shen, 2020). Most stations in the area were installed in phase I of the project in 1999. Most of the stations in the area are campaign GNSS sites that have existed for almost 20 years. The sites were measured twice a year resulting in horizontal velocities with low uncertainties. Wang and Shen (2020) present the latest horizontal velocity field for the area, combining data from continuous and campaign stations from both CMOMOC and regional networks. Their data are published in both ITRF2008 and a Eurasia-fixed reference frame and have an average uncertainty of 0.2 mm/yr. Vertical velocities are available from Liang et al. (2013) in both ITRF2008 and a stable northern neighbours reference frame, with an average uncertainty of 1.5 mm/yr. The stable northern neighbours reference is relative to the average vertical velocity from three continuous stations in the stable Alashan, Ordos and Mon-

golia blocks to highlight the relative vertical motion within the Tibetan Plateau (Liang et al., 2013). As the horizontal components are orthogonal to the vertical component and the reference frame transformations in the horizontal and vertical components are independent, we combine the horizontal components in the Eurasia-fixed reference frame from Wang and Shen (2020) with the vertical components in stable northern neighbours reference frame from Liang et al. (2013) to highlight the tectonic signals.

Not all stations with horizontal velocities have associated vertical velocities because Liang et al. (2013) discarded vertical measurements with uncertainty greater than 2.5 mm/yr and from stations in operation for less than 3 years. There are 282 stations with horizontal velocities in the area covered by the InSAR LOS data and 169 of these have an associated vertical velocity. All 23 frames contain at least 10 well-distributed stations and 20 have at least 8 stations with 3D velocities (Fig 4). Only three frames in the southwest, 026A_05526_131313, 106D_05447_131313 and 033D_05503_131313 (Fig 1), have only 2 or 3 3D stations available, but all have good 2D station coverage.

Text S5. Adjusting $\sigma(LOS)$ for velocity decomposition

The $\sigma(LOS)$ maps derived from time series analysis have lower uncertainties around the chosen reference windows (Fig 2o). This is partly due to the inherent better data quality as the references are chosen in high-coherence non-deforming areas, and partly due to the referencing effect that locally suppressed scatters in the time series and potentially distributed the scatter in the reference window to pixels further away. If these $\sigma(LOS)$ maps are used in the velocity decomposition, the LOS entry that happen to be near the local reference of the frame will be weighted more heavily and the low uncertainty will be reflected in the $\sigma(V_E)$ and $\sigma(V_{UN})$ maps.

The conventional approach for propagating such spatially correlated errors through subsequent calculations is via a covariance matrix estimated from semivariograms based on the LOS velocities (i.e., Sudhaus & Jónsson, 2009). However, in the velocity decomposition step, this approach would require all pixels in the map to be decomposed together with a covariance matrix of the dimension of $10^8 \times 10^8$, which is computationally impractical to implement. The signals in the velocity maps also do not always allow the semivariograms to plateau, making the estimation of a sill difficult. Therefore, we performed velocity decomposition pixel by pixel and tried to remove the effect of the local reference on each $\sigma(LOS)$ map.

We first fitted a spherical model (Equation 7) to the bin median values along the uncertainty profile (thick yellow line in Fig S11a), where d is now distance away from the reference point (yellow dot in Fig S11b). As the reference was the mean value of pixels within a 400×400 window of each contributing interferogram, rather than a fixed pixel on the map, we chose the zero distance at the median location of all pixels with $\sigma(LOS)$ in the lowest 2 percentile. To ensure a good profile fit near the nugget, we weighted the spherical model fitting by $1/(std+d/d_{max})$, where std is the standard deviation of $\sigma(LOS)$ in each bin (thin yellow line in Fig S11a) and d_{max} is the longest distance obtained in the frame.

Then, we scaled up the profile to the sill level by multiplying each scatter point by the ratio between the sill and the best-fit spherical model evaluated at the same distance (red line in Fig S11a). Thanks to the non-zero nugget resulting from the window referencing of the inteferograms, no extreme uncertainty values formed around the reference after scaling. The scatter and the $\sigma(LOS)$ values become more uniform across the scaled

uncertainty profile (Fig S11c). The region around the reference window in the scaled $\sigma(LOS)$ map (Fig S11d) no longer show an uncertainty dip. However, the uncertainty variation characteristic of the quality of time series at each pixel is retained. After the scaled $\sigma(LOS)$ are propagated through the velocity decomposition, the $\sigma(V_E)$ and $\sigma(V_U)$ maps obtained no longer show local referencing effects, but instead, represent uncertainties with velocities referenced in the far field (Fig S14b and Fig S16d).

Text S6. One-Stage Velocity Decomposition with Interpolated GNSS V_N

We compare the two-stage velocity decomposition described in the main text, where V_E and V_{UN} are obtained first from LOS velocity maps before V_U is obtained from V_{UN}, with the conventional approach where the interpolated V_N from GNSS is first taken out of the LOS before V_E and V_U are decomposed in a one stage.

$$\begin{bmatrix} \frac{1}{\sigma(a_0)}(LOS_{a_0} - V_N(sin(\phi_{a_0})sin(\theta_{a_0})) \\ \frac{1}{\sigma(a_1)}(LOS_{a_1} - V_N(sin(\phi_{a_0})sin(\theta_{a_0})) \\ \frac{1}{\sigma(d_0)}(LOS_{d_0} - V_N(sin(\phi_{d_0})sin(\theta_{d_0})) \\ \frac{1}{\sigma(d_1)}(LOS_{d_1} - V_N(sin(\phi_{d_1})sin(\theta_{d_1})) \end{bmatrix} = \begin{bmatrix} \frac{1}{\sigma(a_0)}(-cos(\phi_{a_0})sin(\theta_{a_0}) \;\; cos(\theta_{a_0})) \\ \frac{1}{\sigma(a_1)}(-cos(\phi_{a_1})sin(\theta_{a_1}) \;\; cos(\theta_{a_1})) \\ \frac{1}{\sigma(d_0)}(-cos(\phi_{d_0})sin(\theta_{d_0}) \;\; cos(\theta_{d_0})) \\ \frac{1}{\sigma(d_1)}(-cos(\phi_{d_1})sin(\theta_{d_1}) \;\; cos(\theta_{d_1})) \end{bmatrix} \begin{bmatrix} V_E \\ V_U \end{bmatrix} \tag{6}$$

where $\sigma(k) = \sqrt{\sigma(LOS_k)^2 - (\sigma(V_N)sin(\phi_k)sin(\theta_k))^2}$ for k in a_0, a_1, d_0 and d_1. The $\sigma(V_E)$ is similarly obtained by taking the square-root of the diagonal terms of the covariance matrix assuming independent measurements in the data vector.

The differences between the V_E and $\sigma(V_E)$ obtained by these two methods are shown in Fig S12. The V_E difference map shows a systematic variation of the differences along the range direction, with zero difference along the north-south axis where the incidence angles θ between the ascending and descending tracks are equal. The $\sigma(V_E)$ difference map shows a spatial pattern that reflects the distribution of the GNSS stations where the uncertainty

of the V_E map obtained by the one-stage decomposition increases away from the GNSS stations. Overall, the differences between the two V_E maps average to 0.01±0.03 mm/yr, way below the ∼1 mm/yr uncertainty level that we are working with. The differences between the two $\sigma(V_E)$ maps average to 0.004±0.007 mm/yr, again negligible, suggesting both methods can be used without affecting the final results.

References

Chen, P., Shi, W., Liu, Y., & Cao, X. (2022). Slip rate deficit partitioned by fault-fold system on the active Haiyuan fault zone, Northeastern Tibetan Plateau. *Journal of Structural Geology*, *155*(January), 104516. doi: 10.1016/j.jsg.2022.104516

Daout, S., Doin, M.-P., Peltzer, G., Socquet, A., & Lasserre, C. (2017). Large-scale InSAR monitoring of permafrost freeze-thaw cycles on the Tibetan Plateau. *Geophysical Research Letters*, *44*(2), 901-909. doi: 10.1002/2016GL070781

Diao, F., Xiong, X., Wang, R., Walter, T. R., Wang, Y., & Wang, K. (2019). Slip Rate Variation Along the Kunlun Fault (Tibet): Results From New GPS Observations and a Viscoelastic Earthquake-Cycle Deformation Model. *Geophysical Research Letters*, *46*(5), 2524–2533. doi: 10.1029/2019GL081940

Doin, M. P., Twardzik, C., Ducret, G., Lasserre, C., Guillaso, S., & Jianbao, S. (2015). InSAR measurement of the deformation around Siling Co Lake: Inferences on the lower crust viscosity in central Tibet. *Journal of Geophysical Research: Solid Earth*, *120*(7), 5290–5310. doi: 10.1002/2014JB011768

Gan, W., Zhang, P., Shen, Z. K., Niu, Z., Wang, M., Wan, Y., ... Cheng, J. (2007). Present-day crustal motion within the Tibetan Plateau inferred from GPS measurements. *Journal of Geophysical Research: Solid Earth*, *112*(8), 1–14. doi:

10.1029/2005JB004120

Karra, K., Kontgis, C., Statman-Weil, Z., Mazzariello, J., Mathis, M., & Brumby, S. (2021). Global land use/land cover with Sentinel-2 and deep learning. In *Igarss 2021-2021 ieee international geoscience and remote sensing symposium. ieee.*

Liang, S., Gan, W., Shen, C., Xiao, G., Liu, J., Chen, W., ... Zhou, D. (2013). Three-dimensional velocity field of present-day crustal motion of the Tibetan Plateau derived from GPS measurements. *J. Geophys. Res. Solid Earth*, *118*, 5722–5732. doi: 10.1002/2013JB010503

López-Quiroz, P., Doin, M. P., Tupin, F., Briole, P., & Nicolas, J. M. (2009). Time series analysis of Mexico City subsidence constrained by radar interferometry. *Journal of Applied Geophysics*, *69*(1), 1–15. doi: 10.1016/j.jappgeo.2009.02.006

Sudhaus, H., & Jónsson, S. (2009). Improved source modelling through combined use of InSAR and GPS under consideration of correlated data errors: Application to the June 2000 Kleifarvatn earthquake, Iceland. *Geophysical Journal International*, *176*(2), 389–404. doi: 10.1111/j.1365-246X.2008.03989.x

Wang, M., & Shen, Z.-K. (2020). Present-Day Crustal Deformation of Continental China Derived From GPS and Its Tectonic Implications. *Journal of Geophysical Research: Solid Earth*, *125*(2). doi: 10.1029/2019JB018774

Wright, T. J., Elliott, J. R., Wang, H., & Ryder, I. (2013). Earthquake cycle deformation and the Moho: Implications for the rheology of continental lithosphere. *Tectonophysics*, *609*, 504–523. doi: 10.1016/j.tecto.2013.07.029

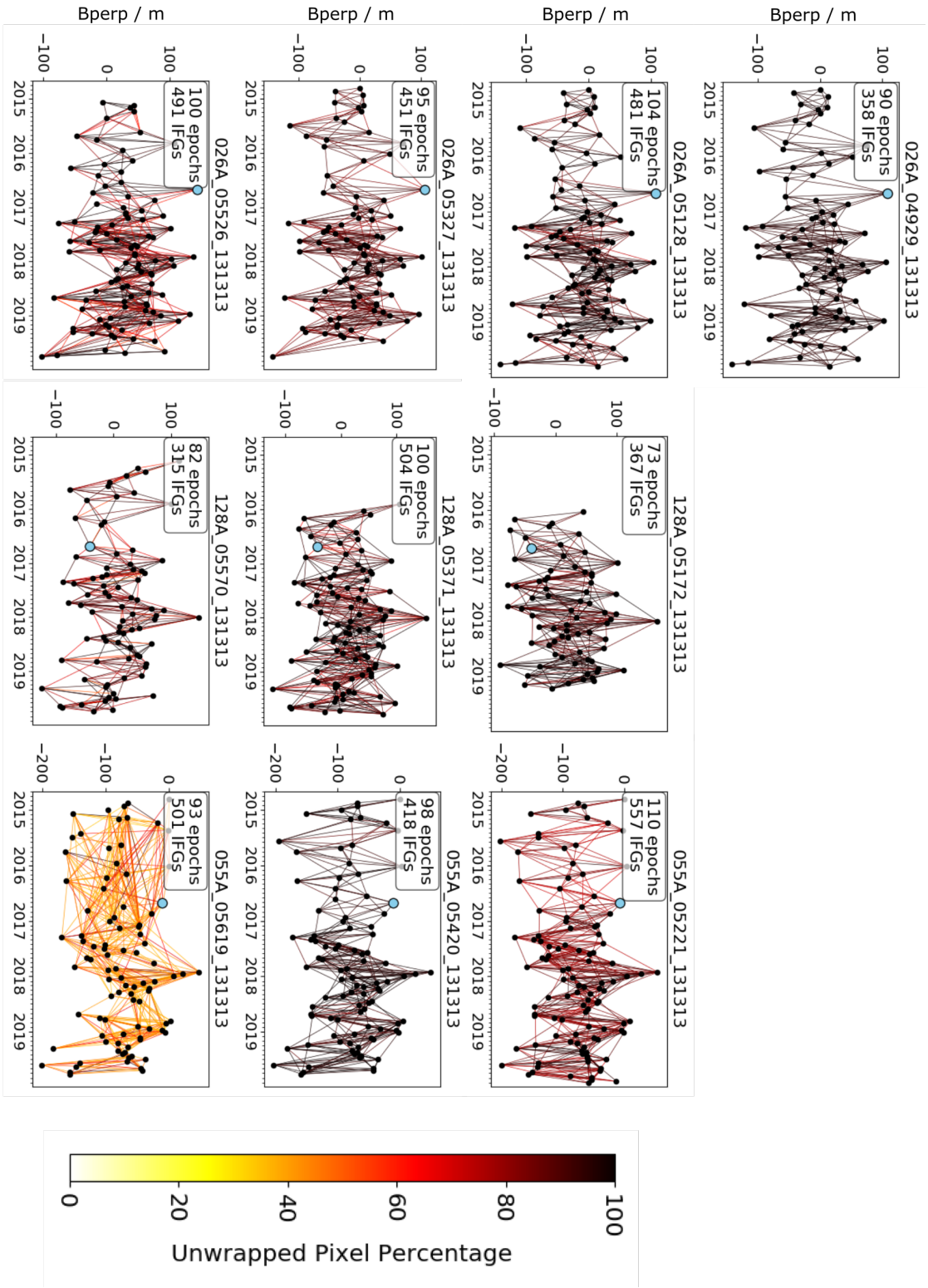

Figure S1. Perpendicular baseline plots for the final time series of ascending frames. Black dots represent all the acquisition dates with their perpendicular baseline. Blue dot in each frame represents the primary epoch to which imagery from other epochs are coregistered. Each line segment represents an interferogram (interferogram) between two acquisition dates with a colour scale representing the percentage of pixels unwrapped out of all pixels in the frame.

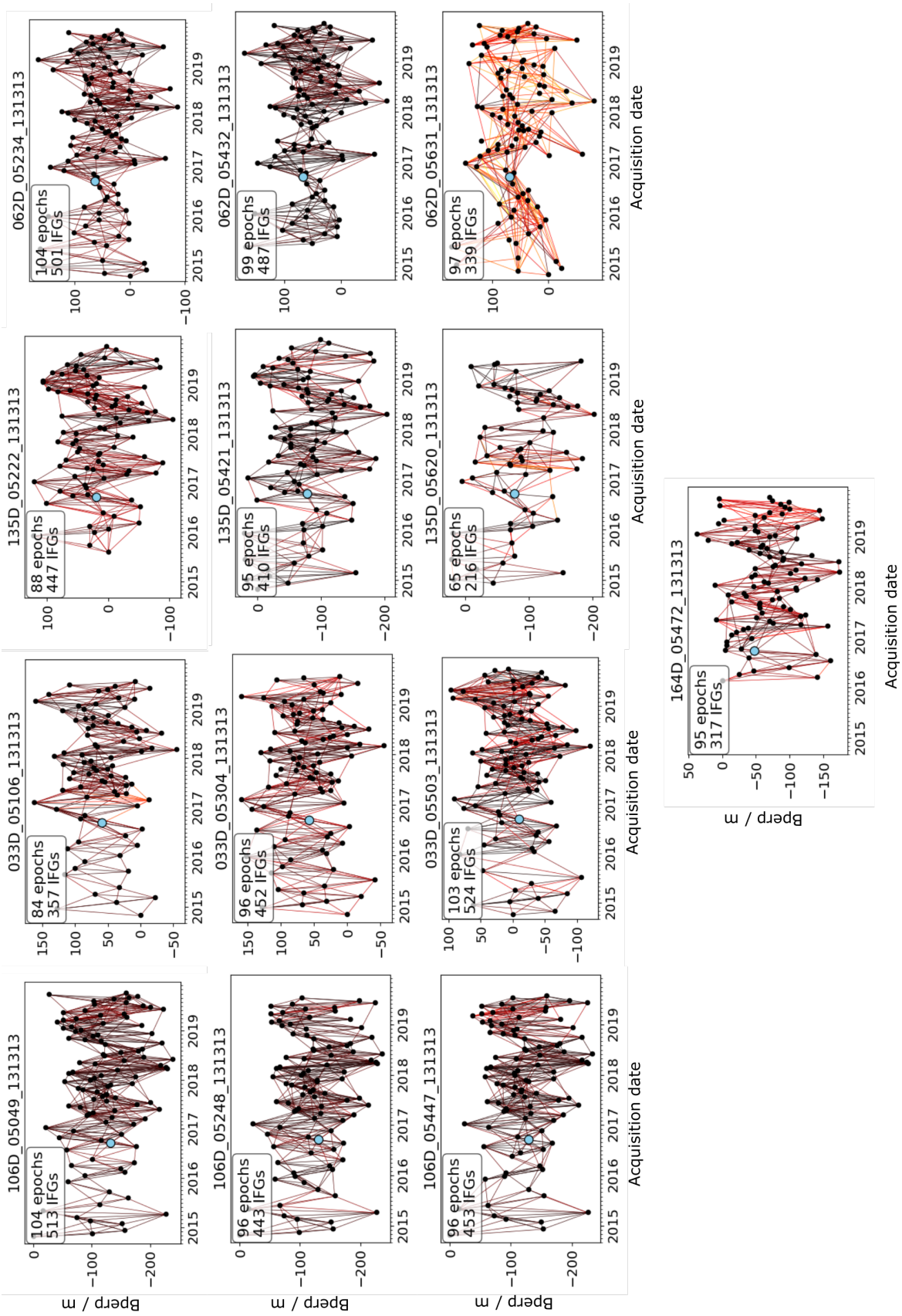

Figure S2. Same as in Fig S1 but for the descending frames.

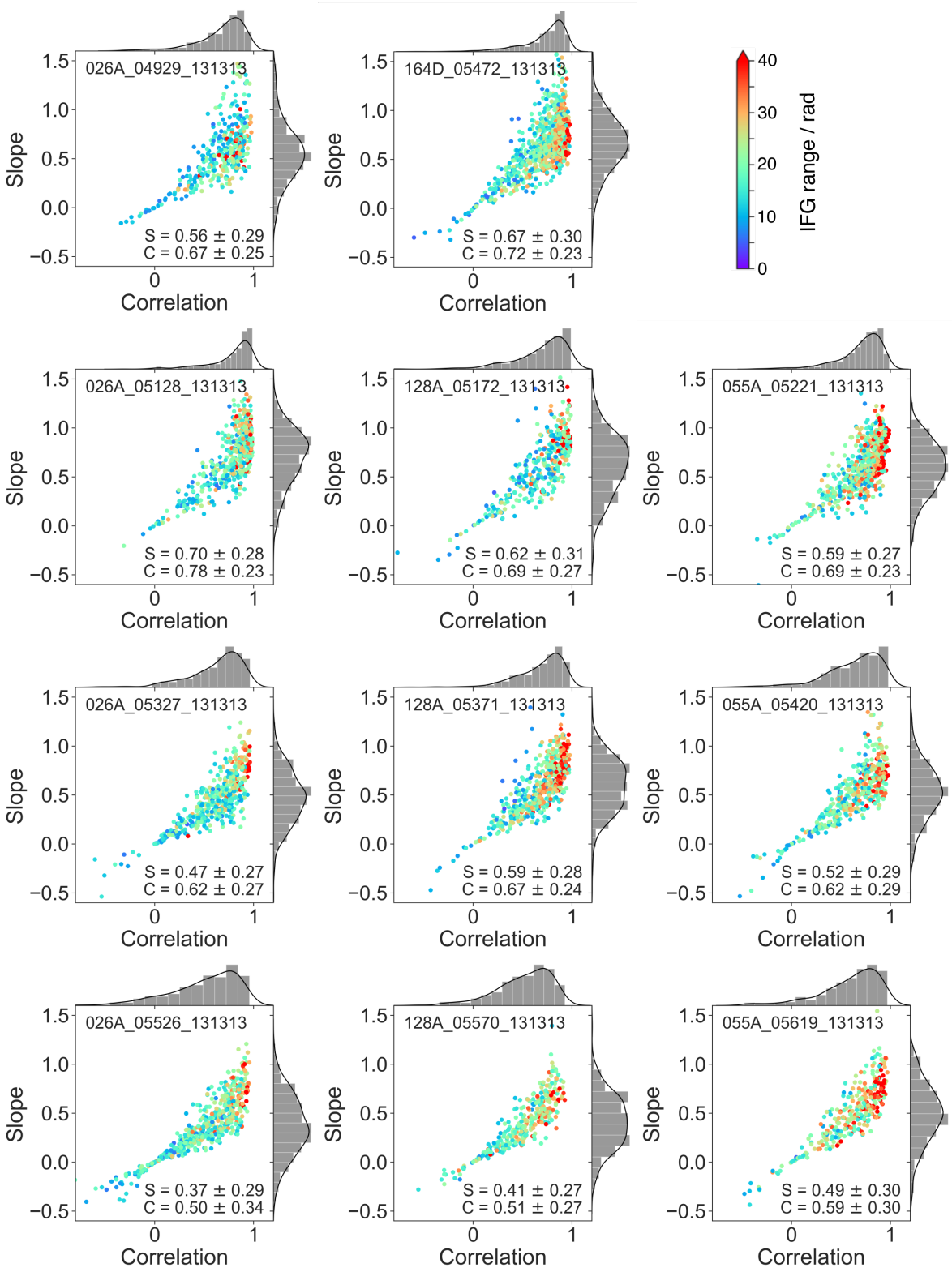

Figure S3. Joint plots between slope and correlation from the scatter plots between GACOS LOS and unwrapped interferogram (Fig 2c) for all interferograms in all ascending frames and frame 164D_05472_131313. The colour of the scatter points represent the amplitude range (difference between the 99.7 percentile and 0.03 percentile of the pixel values) of the corresponding interferogram. The S and C labels in each panel stand for slope and correlation with their mean and standard deviations for each frame.

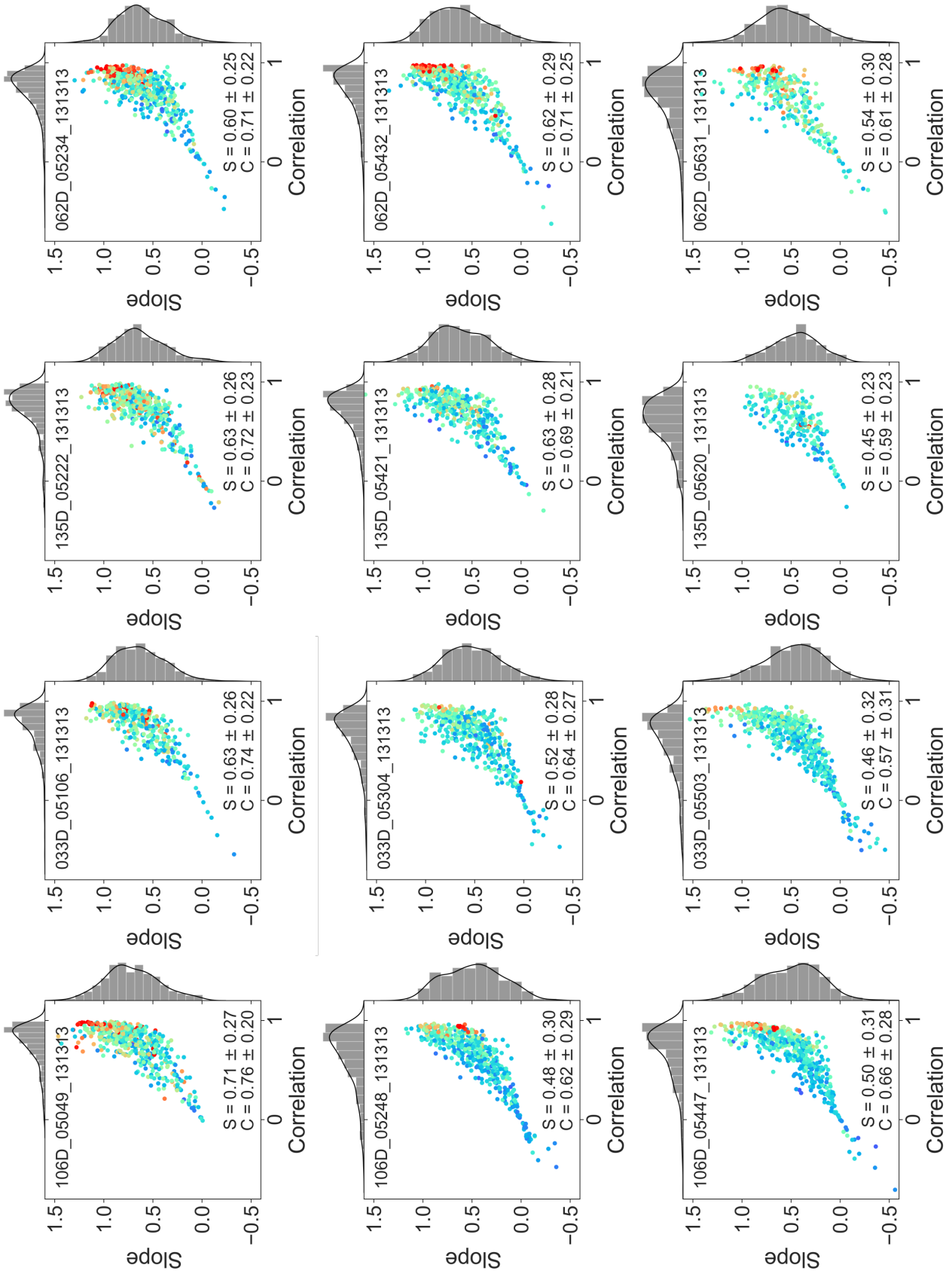

Figure S4. Same as in Fig S3 but for the rest of the descending frames.

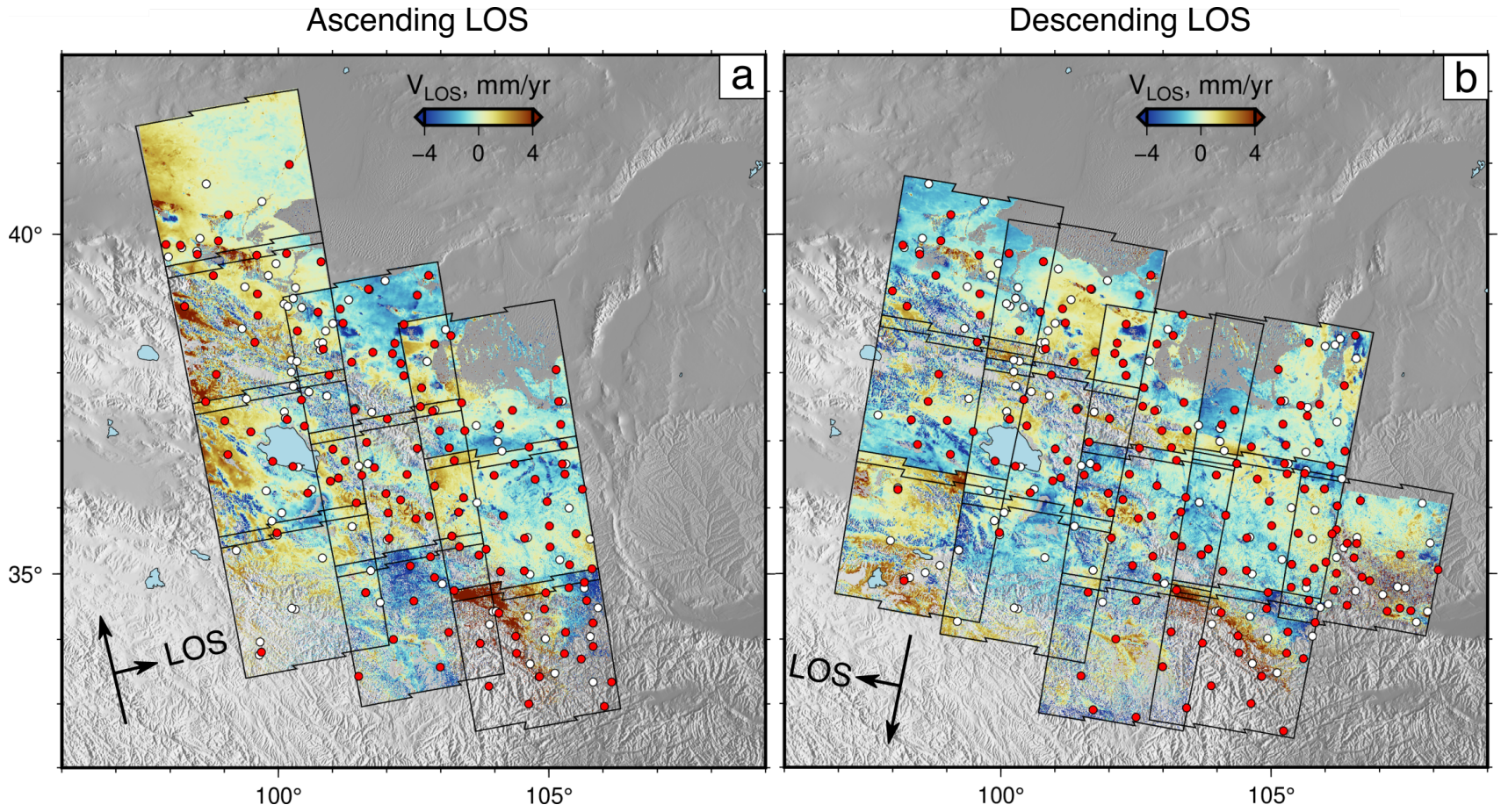

Figure S5. Internally referenced (a) ascending and (b) descending geocoded and cleaned LOS velocity maps merged by placing southern frames on top of northern frames and then eastern tracks on top of western tracks. Red dots are GNSS stations with both horizontal and vertical (3D) velocities and white dots are GNSS stations with horizontal (2D) velocities only. All horizontal GNSS velocities are taken from Wang and Shen (2020) and all vertical GNSS velocities are taken from Liang et al. (2013).

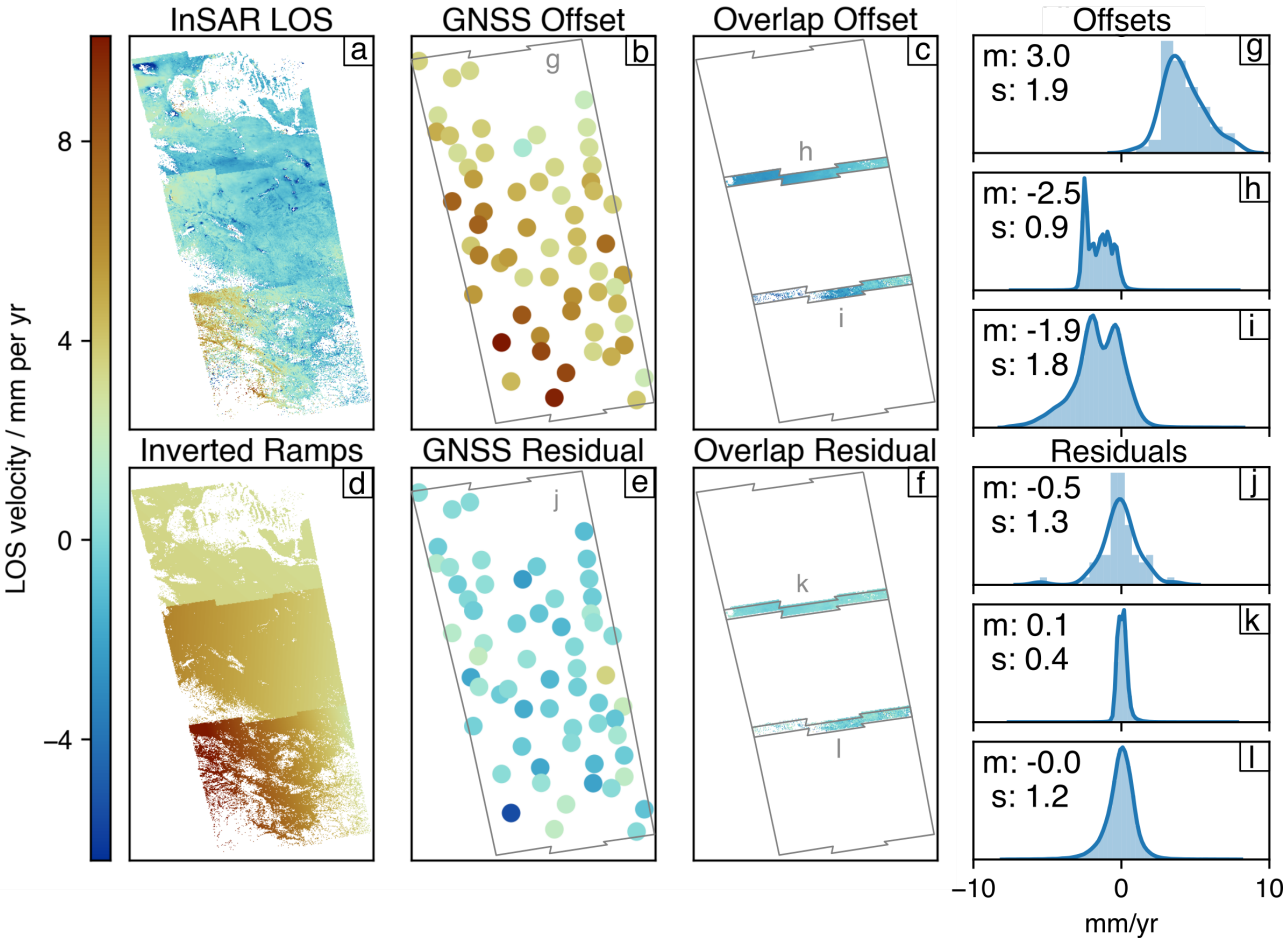

Figure S6. An example from track 055A to illustrate the results of the joint inversion method. (a) Individually referenced LOS velocity frames, same as the eastern track in Fig S5a. (b) Differences between GNSS LOS and the corresponding InSAR LOS in (a). (c) Differences in InSAR frame overlaps obtained by subtracting the southern frame from the northern frame. (d) Ramps inverted from the offsets in (b) and (c) to be subtracted from (a). (e,f) Model residuals after the InSAR LOS are adjusted by the inverted ramps in (d). (g-l) Histograms of the data labelled in panels b, c, e and f, with m = mode and s = standard deviation.

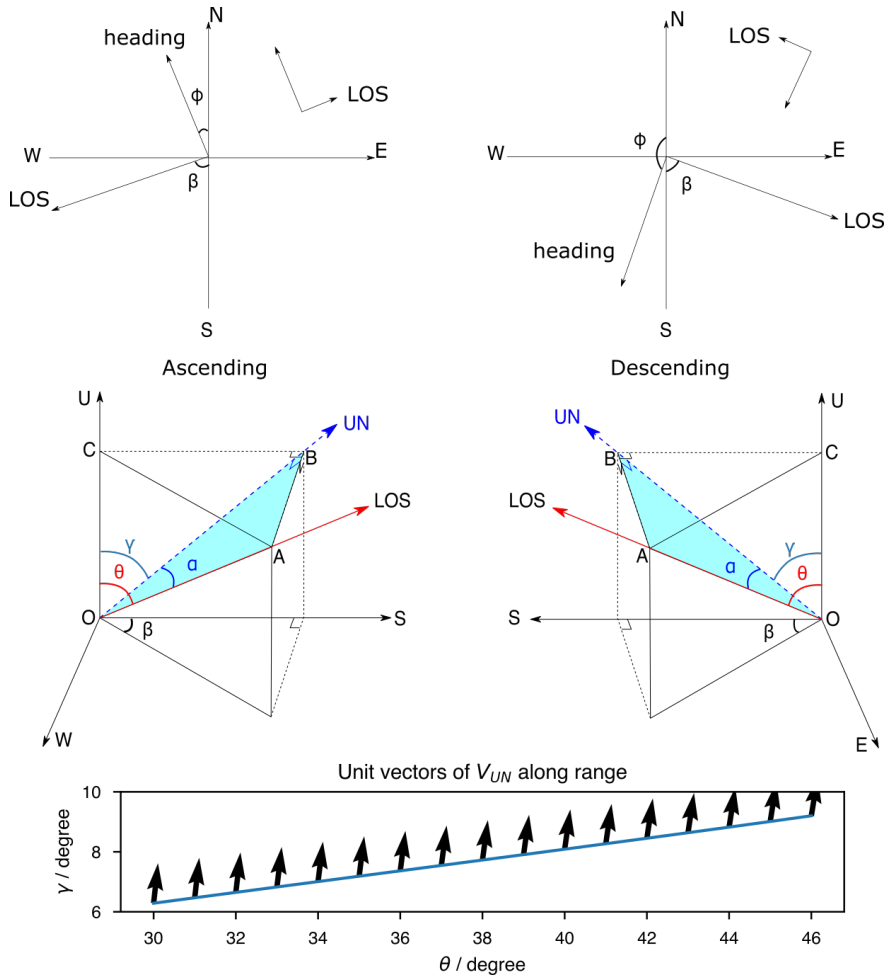

Ascending:
$\phi \sim -10$
$\beta = 180 - 90 + \phi = \phi + 90$
$\sin(\beta) = \sin(\phi+90) = \cos(\phi)$
$V_{LOS} = -V_E \cos(-\phi) \sin(\theta) + (-V_N)\sin(-\phi)\sin(\theta) + V_U \cos(\theta)$
$= -V_E \cos(\phi) \sin(\theta) + V_N \sin(\phi)\sin(\theta) + V_U \cos(\theta)$

Descending:
$\phi \sim -170$
$\beta = 90 - (\phi + 180) = - (\phi + 90)$
$\sin(\beta) = -\sin(\phi+90) = -\cos(\phi)$
$V_{LOS} = V_E \cos(180+\phi) \sin(\theta) + (-V_N)\sin(180+\phi)\sin(\theta) + V_U \cos(\theta)$
$= -V_E \cos(\phi) \sin(\theta) + V_N \sin(\phi)\sin(\theta) + V_U \cos(\theta)$

Geometry:
$AB = OA \sin(\alpha) = OA \sin(\theta) \sin(\beta)$
so, $\sin(\alpha) = \sin(\theta) \sin(\beta)$
$\cos(\alpha) = \text{sqrt}(1 - \sin^2(\alpha))$
$= \text{sqrt}(1 - \sin^2(\theta) \sin^2(\beta))$
$= \text{sqrt}(1 - \sin^2(\theta) \cos^2(\phi))$

Decomposition:
$V_{LOS} = -V_E \cos(\phi) \sin(\theta) + V_N \sin(\phi) \sin(\theta) + V_U \cos(\theta)$
$= -V_E \cos(\phi) \sin(\theta) + V_{UN} \cos(\alpha)$
$= -V_E \cos(\phi) \sin(\theta) + V_{UN} \text{sqrt}(1-\sin^2(\theta)\cos^2(\phi))$

so, $V_{UN} = (V_N \sin(\phi) \sin(\theta) + V_U \cos(\theta)) / \text{sqrt}(1- \sin^2(\theta) \cos^2(\phi))$

Small variation in γ:
As $V_{UN} = -V_N \sin(\gamma) + V_U \cos(\gamma)$, we can evaluate γ through:
$\tan(\gamma) = \sin(\gamma) / \cos(\gamma) = -\sin(\phi) \sin(\theta) / \cos(\theta) = -\sin(\phi) \tan(\theta)$
so, $\gamma = \tan^{-1}(-\sin(\phi) \tan(\theta))$ as plotted

Figure S7. Geometry for calculating velocity components from LOS velocities. O=Ground pixel, N=North, E=East, S=South, W=West, U=Up, LOS=Line of sight direction from the point of observation to the satellite, UN=Projection of LOS to the north-up plane. OA=Combined LOS contributions from V_U and V_N. OB=Projection of OA onto the UN plane. ϕ=Negative (heading) angle anti-clockwise from N, θ=Positive (incidence) angle between LOS and U, α=Positive angle between LOS and UN, β=Positive angle between the projection of the LOS onto the horizontal plane and S, γ=Positive angle between UN and U. Arrows in the bottom panel show unit vectors of V_{UN} along range to visually show that variation in γ is negligible along range.

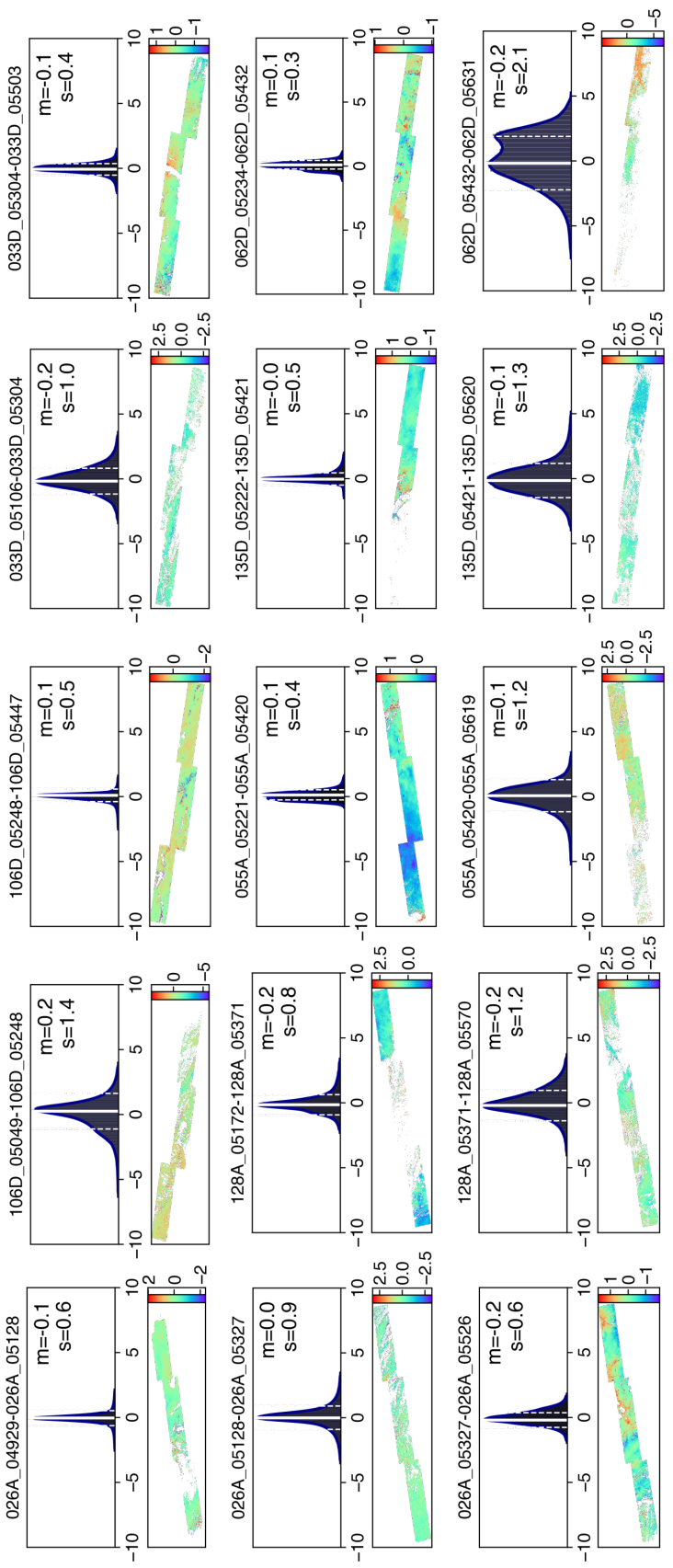

Figure S8. Histograms of pixel differences between frame overlaps along tracks after joint adjustment. m=mode, s=standard deviation.

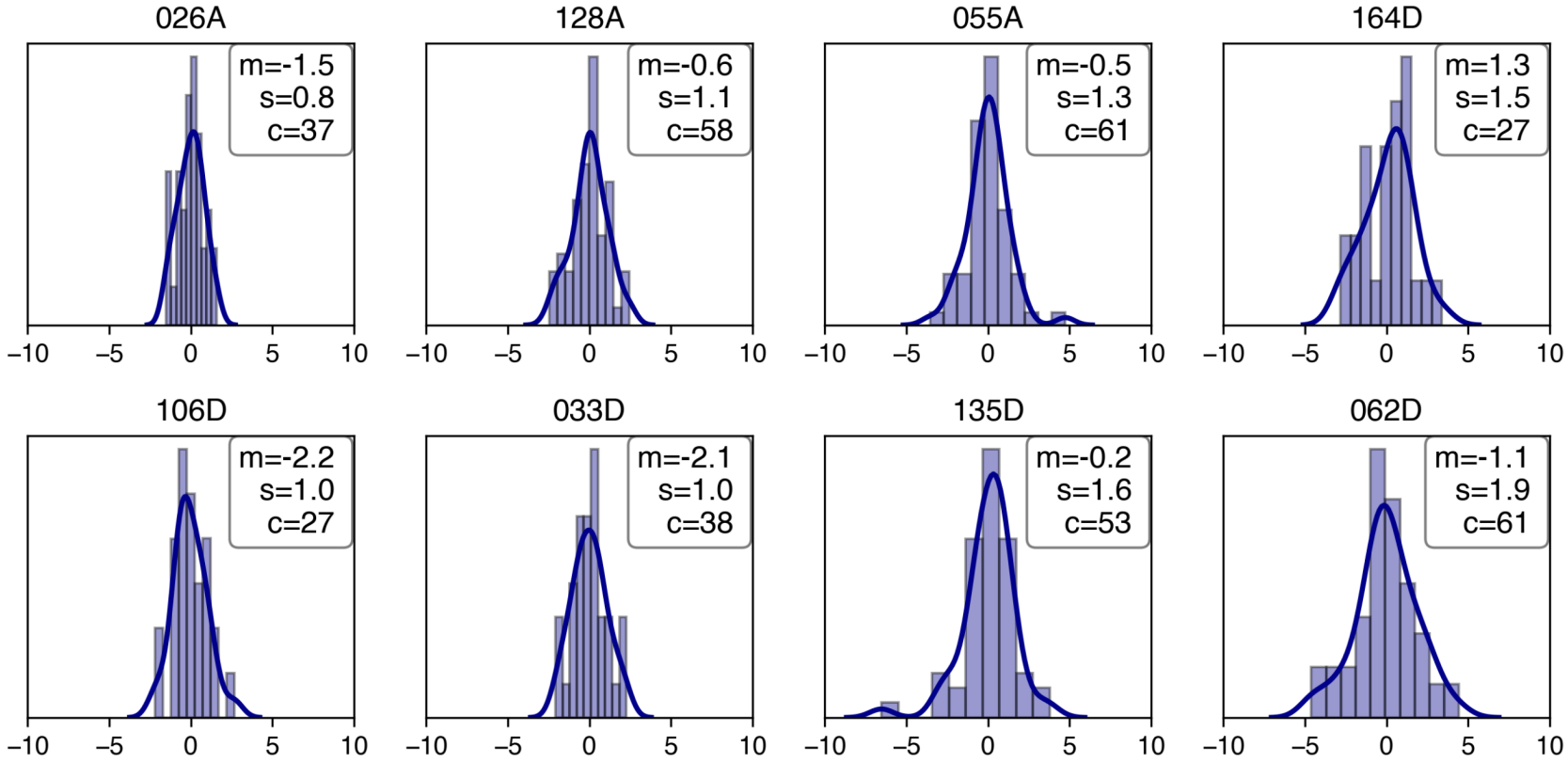

Figure S9. Histograms of residuals between GPS LOS and InSAR LOS in each track after joint adjustment. m=mode, s=standard deviation, c=count of 3D GNSS points in each track.

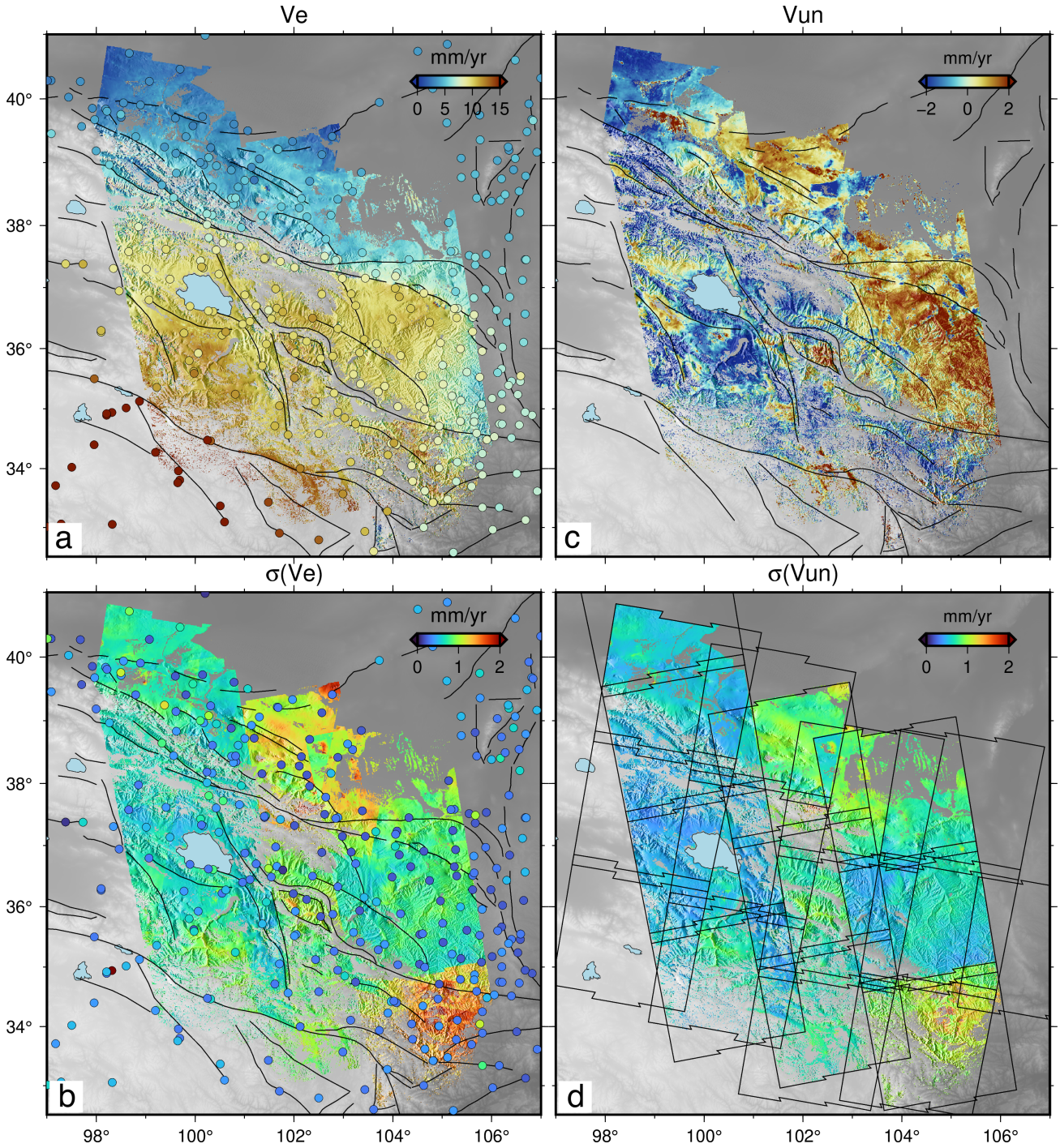

Figure S10. Maps of decomposed V_E and V_{UN} velocity and their associated uncertainty maps $\sigma(V_E)$ and $\sigma(V_{UN})$. Dots in (a-b) are the east component of GNSS velocities and their uncertainties from Wang and Shen (2020) plotted in the same colour map.

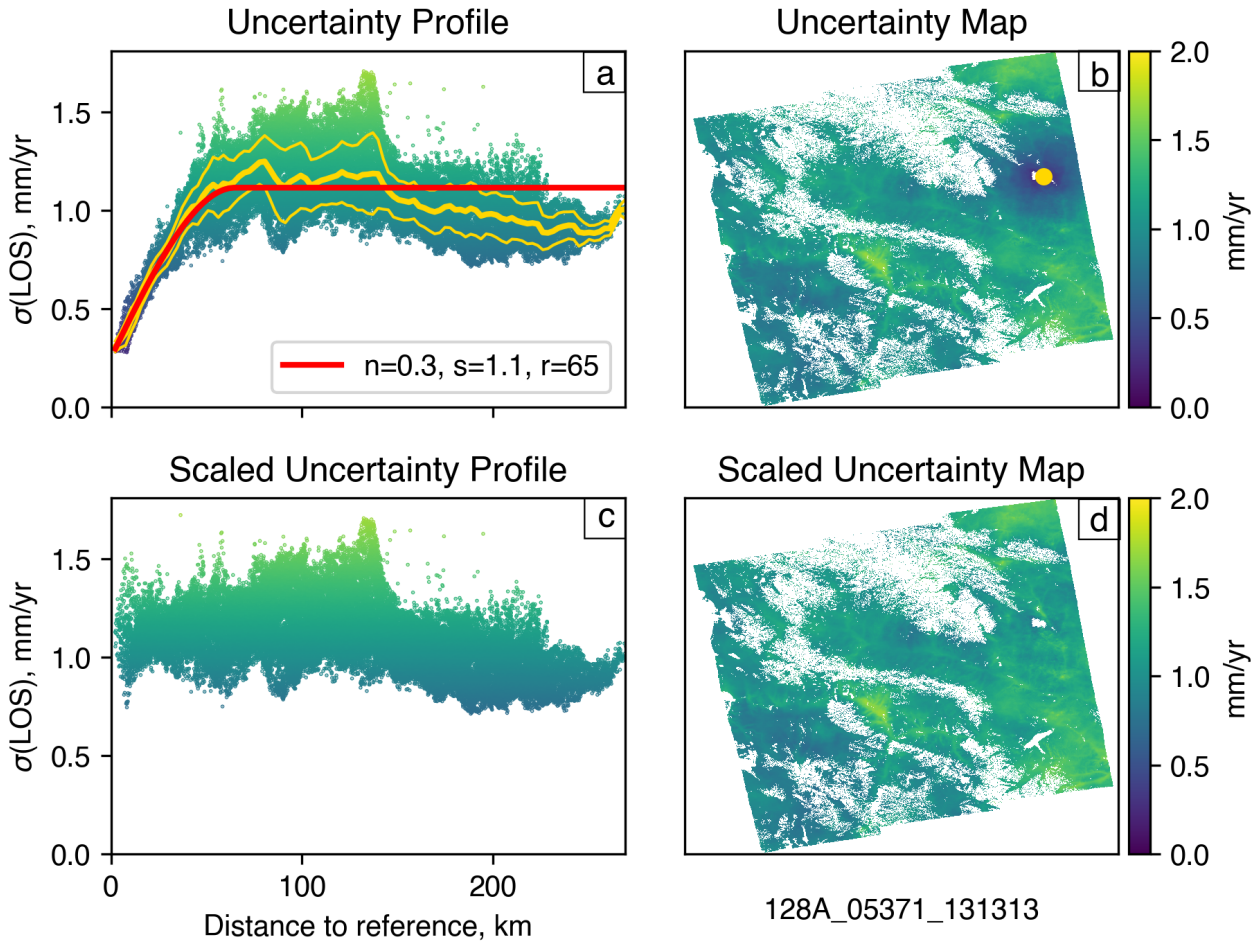

Figure S11. (a) $\sigma(LOS)$ profile against distance away from the reference point indicated by the yellow dot in the $\sigma(LOS)$ map in (b), determined as the median pixel location of pixels with the lowest 2 percent $\sigma(LOS)$ values. In (a), thick and thin yellow lines represent the median and standard deviation evaluated at 100 bin centers, which are used to fit the spherical model in red, with best-fit parameters nugget (n), sill (s) and range (r) labeled. (c) Adjust $\sigma(LOS)$ profile with each scatter point scaled by the ratio between the sill and the best-fit spherical model at given distance. (d) $\sigma(LOS)$ after scaling, with the dip in $\sigma(LOS)$ values removed.

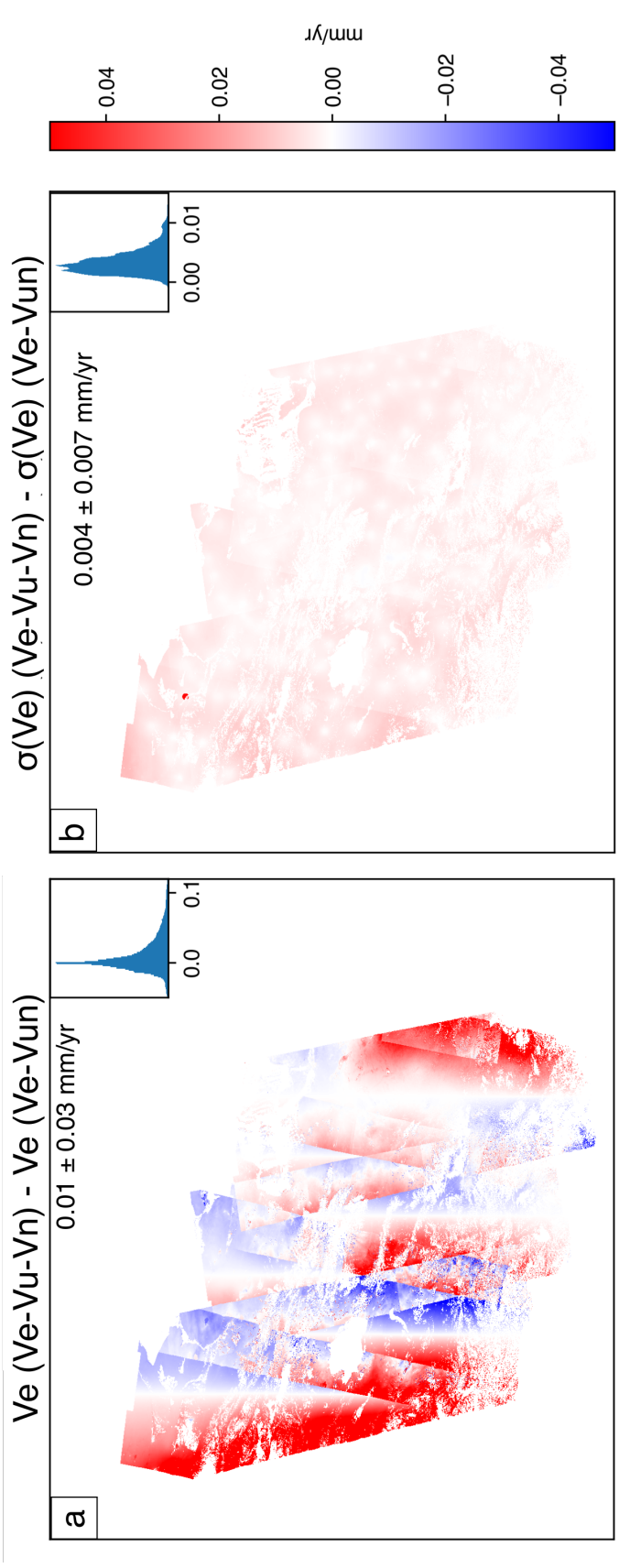

Figure S12. Difference maps and statistical analysis of the differences between the V_E and σV_E maps obtained from method described in Text S6 where the contribution from an interpolated GNSS V_N is first taken out of the LOS velocities to obtain V_E and V_{UN} together and those from the V_E V_{UN} decomposition as described in the main text. Mean and standard deviation of the differences are labeled in each panel.

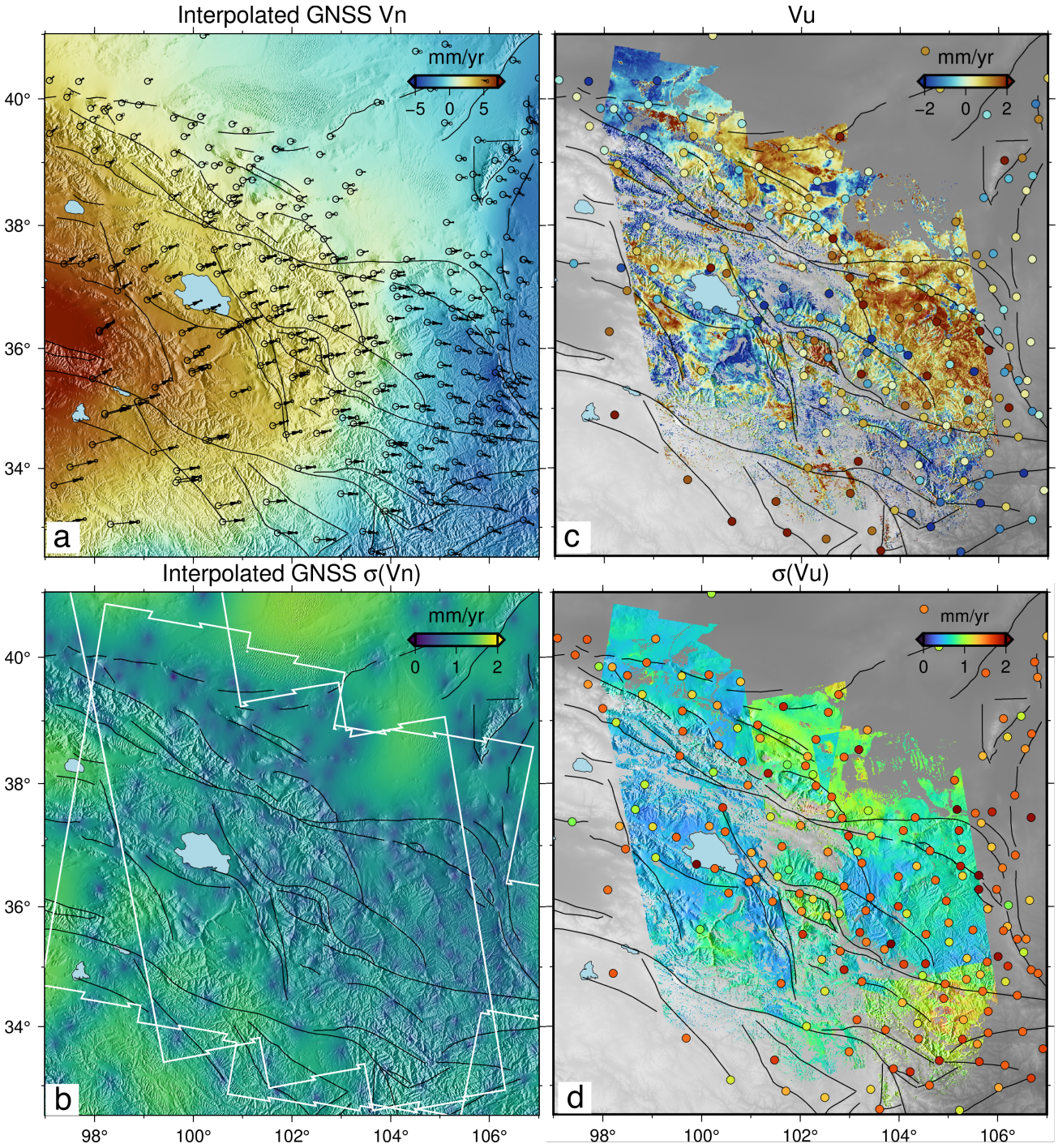

Figure S13. (a-b) Maps of V_N and $\sigma(V_N)$ as interpolated from the north component of the GNSS velocities from Wang and Shen (2020) shown in arrows. (c-d) Resolved maps of V_U and $\sigma(V_U)$, in comparison with the vertical component and uncertainties of the GNSS velocities from (Wang & Shen, 2020) shown as dots in the same colour map.

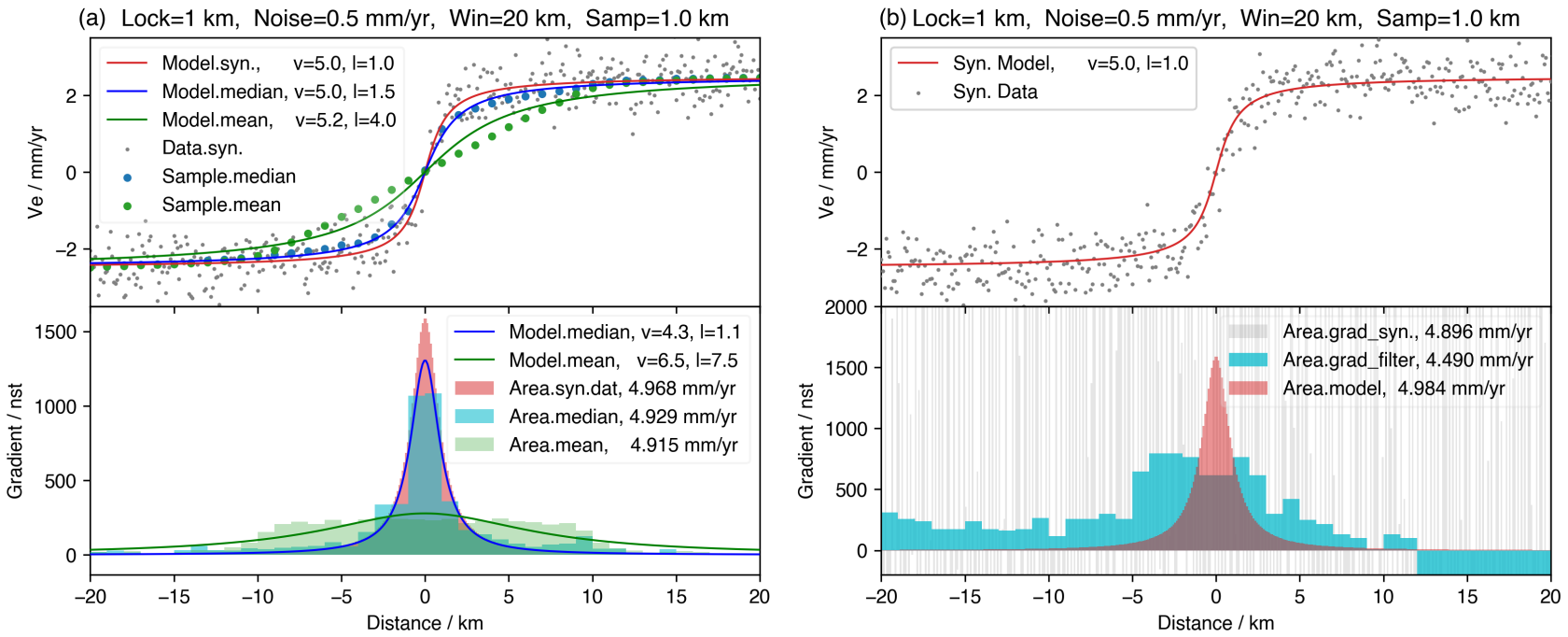

Figure S14. Synthetic test on a 40-km long shallow-locking profile, comparing the effects of (a) median versus mean filtering and of (b) median filtering the raw gradients instead of median filtering the velocity data. Red line is an arctangent dislocation model with locking depth of 1 km and velocity step of 5 mm/yr, sampled at 100 m resolution. Grey dots are synthetic data with random Gaussian noise at 0.5 mm/yr level added to the red line model. Blue and green dots are grey dots after median and mean filtering, respectively, at 1 km interval and with a 20 km wide filter window. Bar plots show numerically evaluated velocity gradients of the synthetic model (red), synthetic velocity data (grey), at 100 m resolution, and of the median (blue) and mean (green) filtered velocity data at 1 km resolution, labeled with summed bar areas in mm/yr. Blue and green lines are the best-fit velocity profiles and gradient profiles (derivative of arctangent), labeled with inverted velocity (v in mm/yr) and locking depth (l in km).

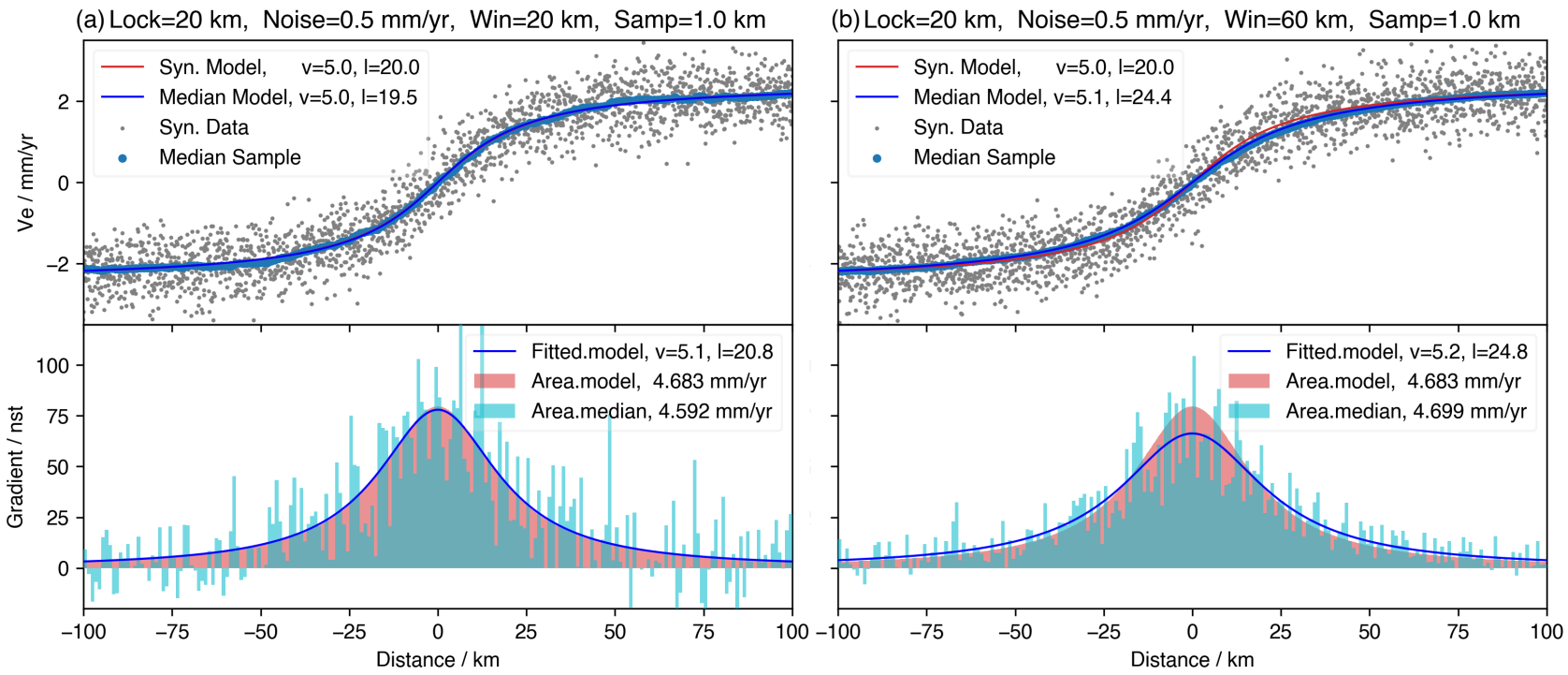

Figure S15. Applying median filters of (a) 20 km and (b) 60 km window sizes to a 200 km-long velocity profile with 20 km fault locking depth, with the same velocity step and noise level as in Fig S14. The longer wavelength of the velocity profile reduces the amplitude, hence the signal-to-noise ratio, of the velocity gradient profile. A 20 km median filter is insufficient to remove noise in the velocity gradient. The negative gradients, when squared, will overestimate the maximum shear and second invariant of the strain rates. A 60 km median filter removes most of the negative gradients, hence when squared, gives a fairer representation of the strain rates.

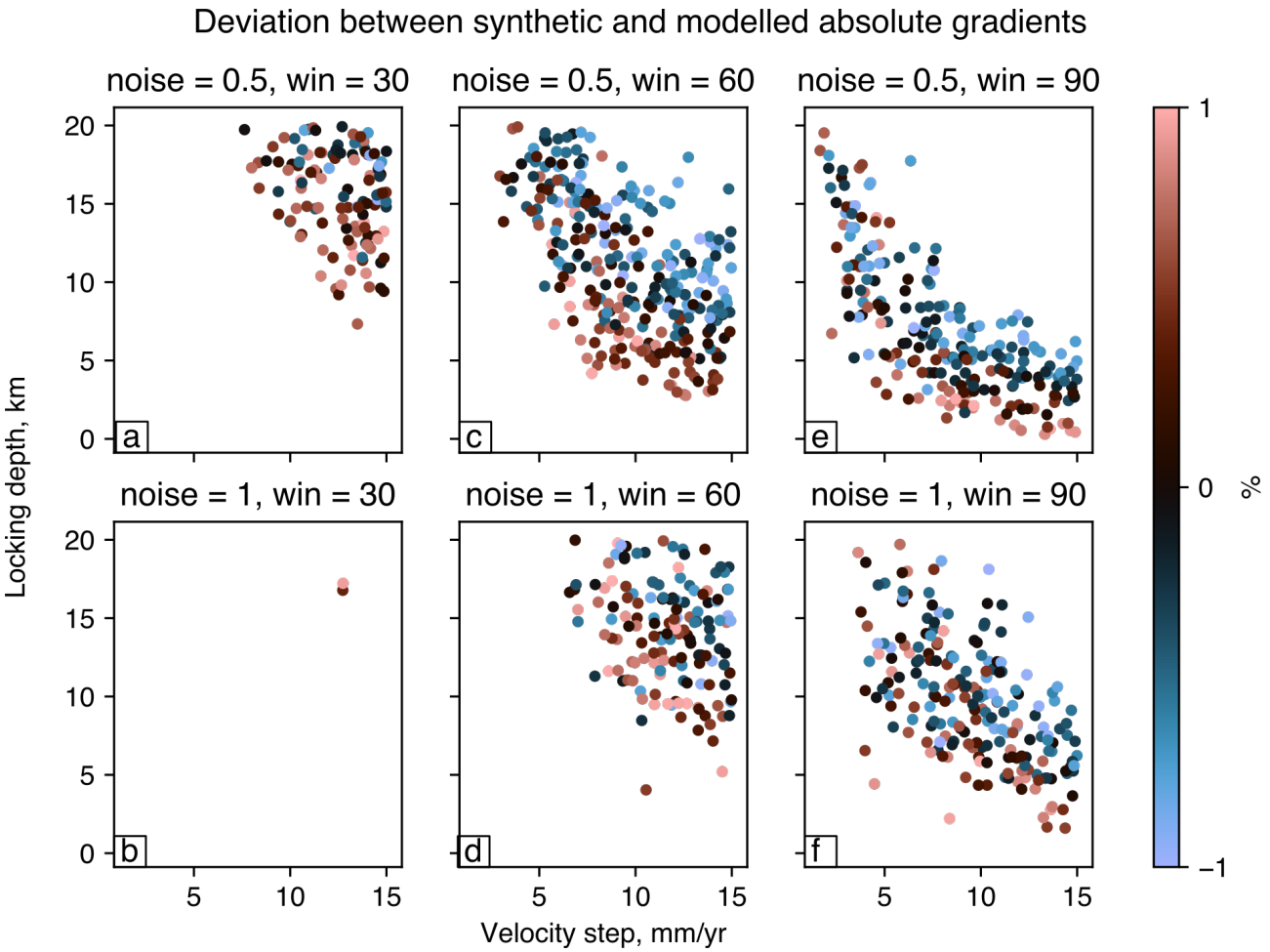

Figure S16. Synthetic tests for the suitability of median filter windows of (a-b) 30 km, (c-d) 60 km and (e-f) 90 km for smoothing synthetic velocity profiles with a range of velocity steps and locking depths simulated with noise levels of (a,c,e) 0.5 mm/yr and (b,d,f)1.0 mm/yr. For each panel, we ran 1000 simulations with random samples of velocity step drawn between 0–15 mm/yr and locking depth drawn between 0-20 km. The scatters only show velocity step and locking depth combinations where the summed absolute velocity gradients (blue bars in Fig S15) deviates from that of the model (red bars in Fig S15) by less than 1%. For typical interseismic locking depths of 13±6 km for Tibet (Wright et al., 2013), the 60 km filter window is suitable for our study region where the Haiyuan Fault is slipping at rates between 4-14 mm/yr (Chen et al., 2022, and references therein) and has InSAR $\sigma(V_E)$ ~0.5 mm/yr (Fig S10b) and the East Kunlun Fault is slipping at rates between 2-13 mm/yr (Diao et al., 2019, and references therein) and has $\sigma(V_E)$ ~1 mm/yr (Fig S10b).

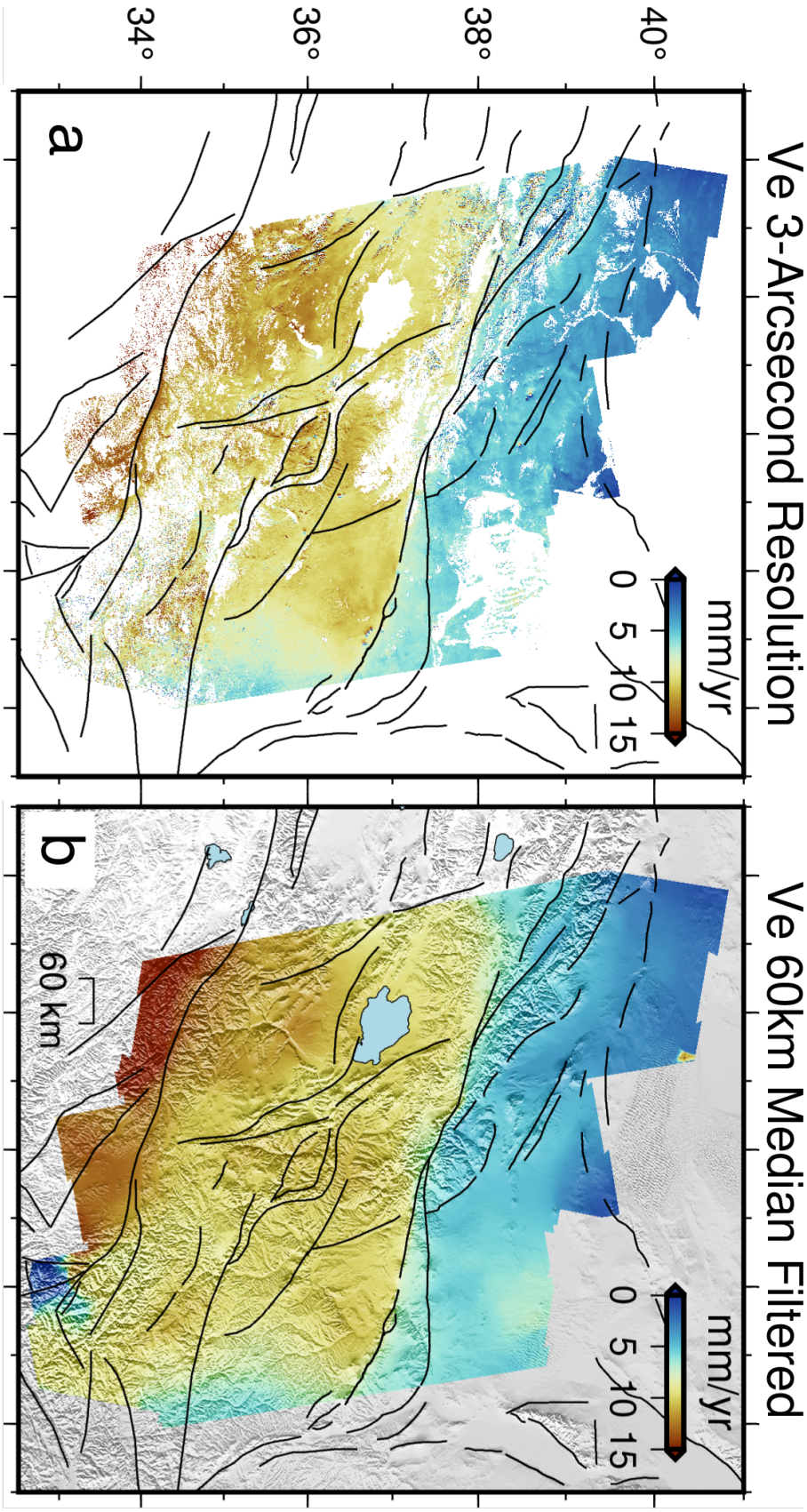

Figure S17. (a) V_E resampled to 3-arcsecond resolution from the original ~100 resolution provided by the resolution of the LOS velocity maps. (b) Median-filtered V_E with a filter window of 60 km.

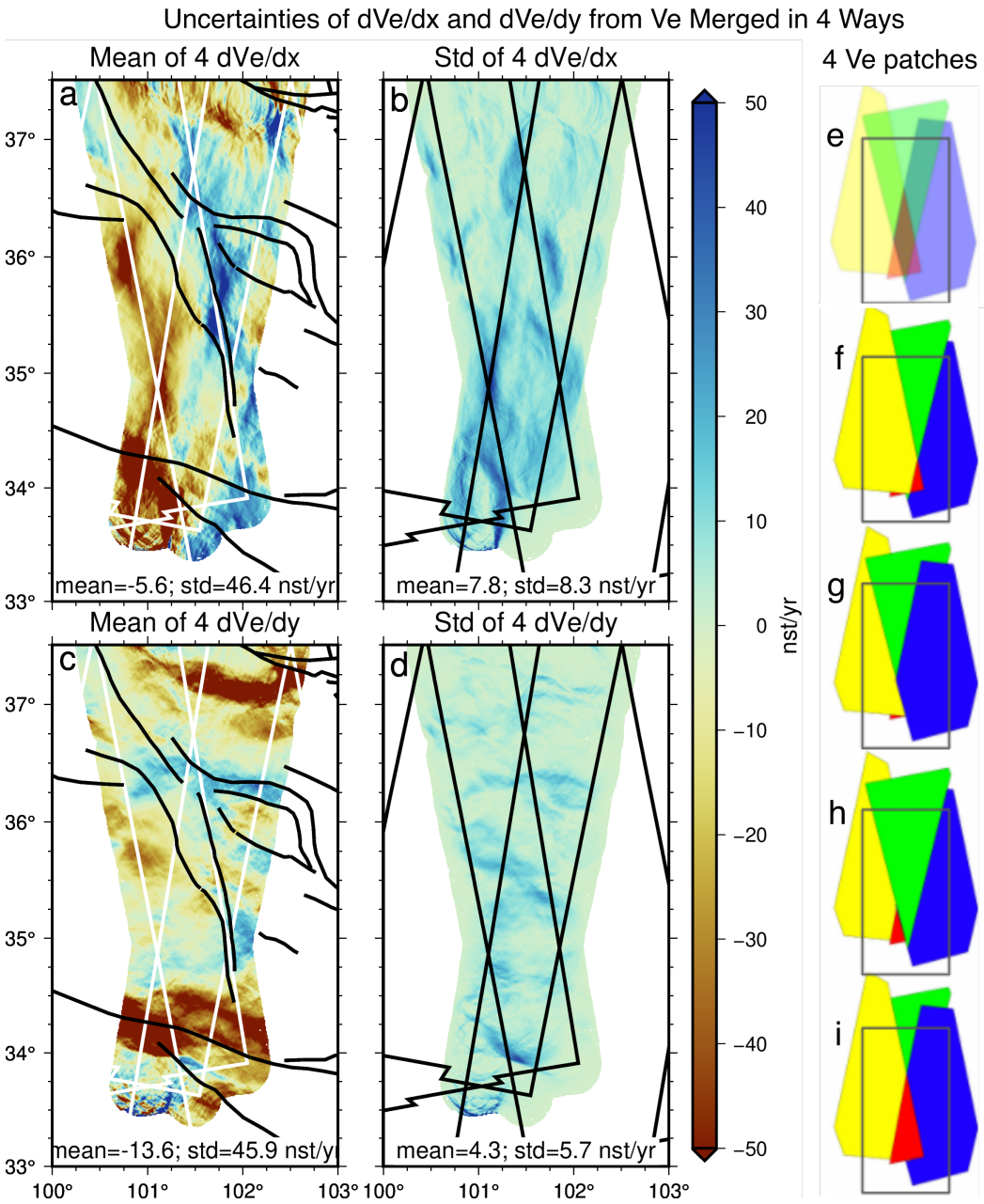

Figure S18. Uncertainties of V_E gradients estimated from four versions of V_E around a region overlapped by two ascending and two descending tracks (026A, 128A, 033D, 135D (Fig 1b,c)). (a, c) Averages of 4 V_E gradients, with faults in black and track boundaries in white. (b, d) Standard deviations of 4 V_E gradients with track boundaries in black. (a-d) only show pixels with changing V_E gradients. We first derived (e) four V_E patches of polygonal shape (yellow, red, green and blue), each obtained through $V_E - V_{UN}$ decomposition from one of the ascending and one of the descending tracks. We then produced four versions of merged V_E by stacking the four V_E patches in four different orders (f-i) which are then filtered before spatial gradients are taken. The grey boxes in (e-i) indicate the plotting region in (a-d).

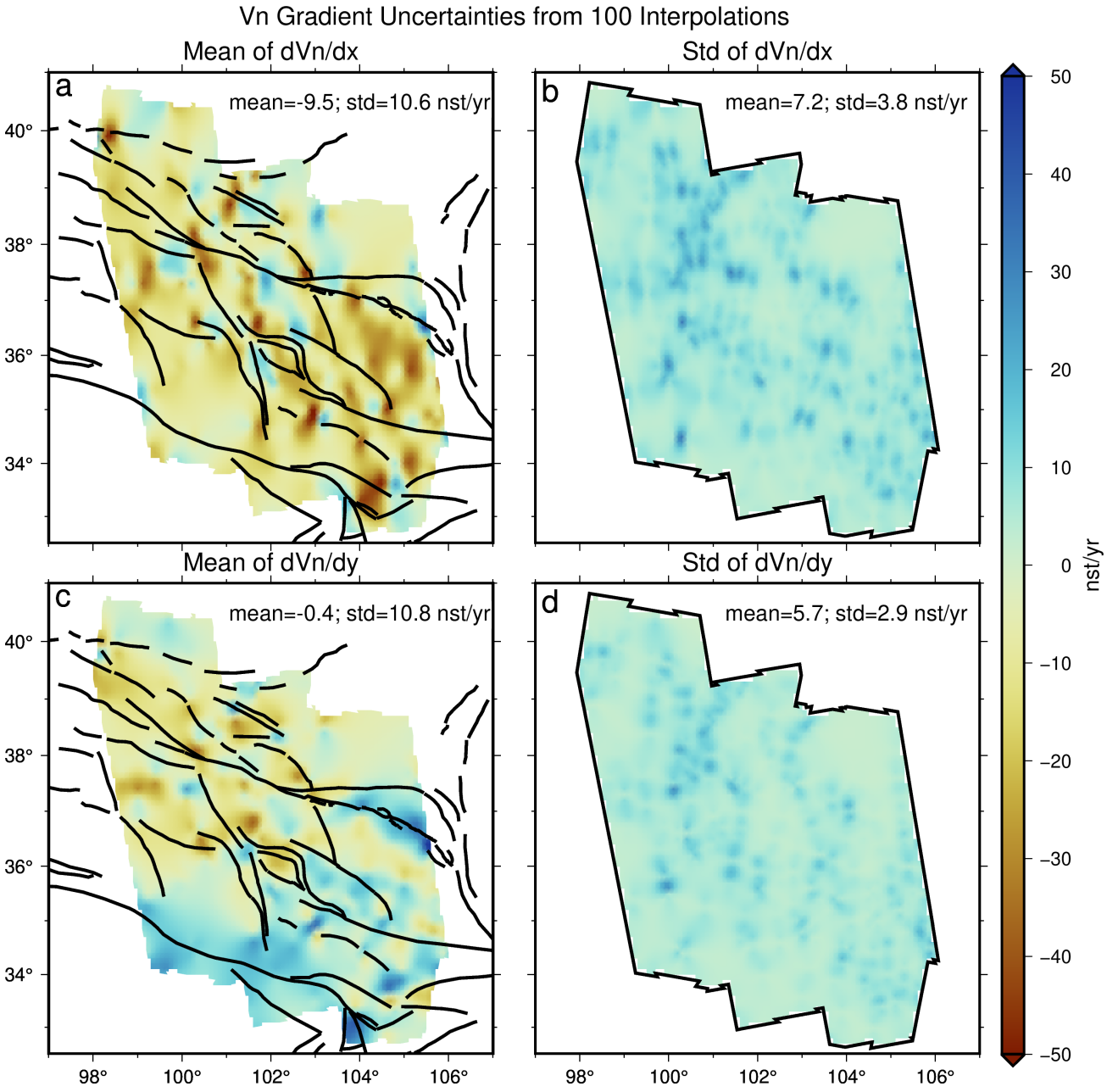

Figure S19. Uncertainties of V_N gradients estimated by interpolating 100 versions of GNSS V_N data sets generated using the Monte Carlo method, each time each GNSS V_N is perturbed by an amount randomly sampled from a Gaussian distribution with its associated σV_N. (a, c) Average of four V_N gradients, with faults in black. (b, d) Standard deviation of four V_N gradients. Pixel statistics labelled in (a-d) are based on pixels within the InSAR data coverage.

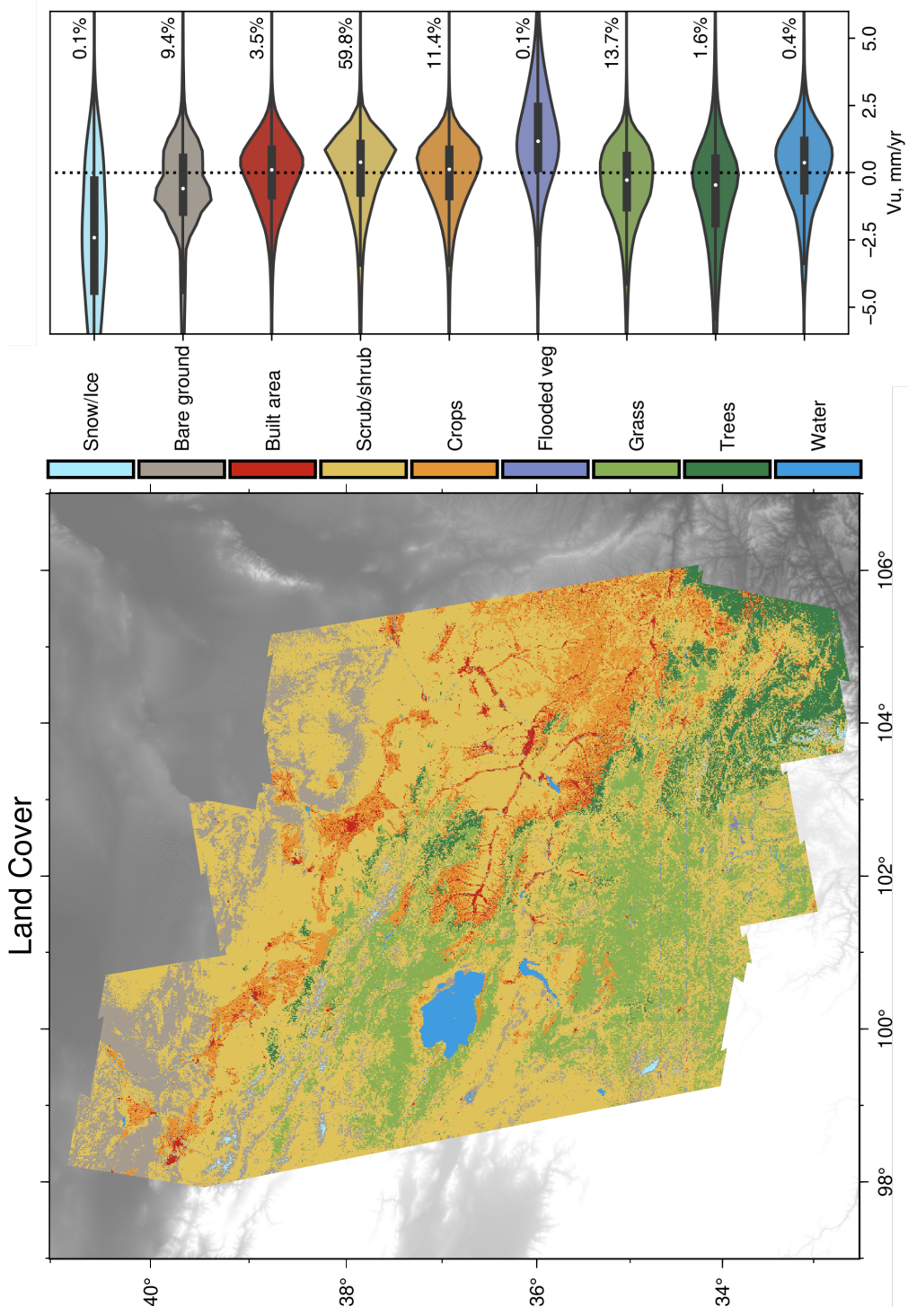

Figure S20. Map of ESRI's global land cover classification (Karra et al., 2021) over the study region, with violin plots between V_U and land cover showing a strong dependency of V_U with water-related land covers (Snow/Ice, Flooded vegetation and Water). The violin-shaped plots on the right show normalised probability density functions of V_U values in each land cover class. The black bars at the center of each violin show the 25-75% range of each distribution and the white dots indicate the median values. Percentage labels at the end of each violin plot show the proportions of V_U pixels of each class in all V_U pixels. SAR signals decorrelate over water surfaces, so most water pixels with V_U measurements are along river and lake banks.